# Tunable laser-generated GHz surface acoustic waves during magnetostructural phase transition in FeRh thin films

Ia. A. Mogunov,<sup>1,\*</sup> A. Yu. Klokov,<sup>2</sup> N. Yu. Frolov,<sup>2</sup> A. V. Protasov,<sup>3</sup> G. E. Zhezlyaev,<sup>3</sup> D. I. Devyaterikov,<sup>3</sup> R. R. Gimaev,<sup>4</sup> V. I. Zverev,<sup>5</sup> and A. M. Kalashnikova<sup>1</sup>

<sup>1</sup> Ioffe Institute, 194021 St. Petersburg, Russia <sup>2</sup> P.N. Lebedev Physical Institute of the RAS, 119991 Moscow, Russia <sup>3</sup> Institute of Metal Physics of the Ural Branch of the RAS, 620108 Ekaterinburg, Russia <sup>4</sup> Faculty of Mechanical Engineering, University of Ljubljana, 1000 Ljubljana, Slovenia <sup>5</sup> Lomonosov Moscow State University, 119991 Moscow, Russia (Dated: November 13, 2025)

Laser-generated surface acoustic waves (SAW) facilitate an efficient information processing in modern spintronics and magnonics. The ability to tune SAW parameters is crucial to achieve an acoustic control over magnonic properties. Such tunability can be achieved in phase-changing magnetic materials accommodating both spin waves and SAWs. A promising material is FeRh alloy, a metallic antiferromagnet at room temperature undergoing a phase transition into ferromagnetic state accompanied by a crystal lattice expansion at 370 K. This transition can also be induced by femtosecond laser pulses. In this paper we use the phase transition in 60 nm Fe<sub>49</sub>Rh<sub>51</sub> film to optically generate pulses of Gigahertz quasi-Rayleigh SAWs. We detect them via photoelastic effect and show that the lattice transformation during phase transition is a dominant strain-generation mechanism for above-threshold excitation. The weight of this contribution rises as the sample is heated closer to AFM-FM transition temperature and 'switches off' when heated above it allowing to control the SAW amplitude. A model based on thermodynamical parameters of Fe<sub>49</sub>Rh<sub>51</sub> shows that the lattice transformation occurring within 95 ps effectively contributes to SAW generation happening at a comparable timescale, while non-equilibrium fast kinetics of the phase transition does not.

## I. INTRODUCTION

Spintronics and magnonics are quickly developing as energy efficient and versatile ways of data manipulation. The most recent advancement constitutes antiferromagnetic spintronics [1–3] promising unprecedentedly fast information processing at THz frequencies and information storage insensitive to external magnetic fields. One of the most energy efficient and versatile ways to control spins is provided by crystal lattice and includes static deformations [4], continuous monochromatic acoustic waves [5], standing acoustic waves [6] and high-frequency strain pulses [7–9]. Surface acoustic waves (SAWs) are proven to interact especially efficiently with magnons [10, 11] allowing coherent control by establishing magnetic polarons [6, 12] as well as other interaction regimes such as Cherenkov radiation of magnons [13]. Magnetoacoustics with SAWs can provide a protected acoustic channel of communication between elements of on-chip magnonic devices [14]. Pulsed laser-generated SAWs [15] in tandem with laser-generated spin waves [16] have recently been successfully employed in magnetoacoustics owing to noncontact generation, wide spectra and high frequencies [12, 14]. Magnonics and magnetoacoustics have also been proposed for unconventional computing [17–20], such as neuromorphic [18], which requires nonlinearities in the system [21]. One way to introduce nonlinearities to magnetoacoustic device is to use a material with the 1st-order phase transition [22] between two magnetically-ordered phases.

A promising candidate for this is FeRh alloy with 47-55 % rhodium content which shows a 1st order phase transition from antiferromagnetic (AFM) to ferromagnetic (FM) phase accompanied by emergence of 0.9  $\mu_B$ magnetization on Rh atom and a 1 % isotropic volume expansion of its cubic lattice [23–26]. For Fe<sub>49</sub>Rh<sub>51</sub> thin films, the thermally induced AFM-FM transition occurs just above room temperature in a range  $T_{PT}$ =360-390 K [27–30] which led to several applications of FeRh in AFM spintronics [31, 32] and as a AFM memory cell [33– 35]. FeRh demonstrates a strong magnetoelastic coupling [36, 37] allowing magnetic-field induced AFM-FM phase transition [28] resulting in a huge volume magnetostriction  $8.2 \times 10^{-3}$  [38, 39]. FeRh alloys are also well-known due to giant magnetocaloric effect [26, 40, 41] and giant magnetoresistance [42]. The ability to trigger the AFM-FM transition in FeRh films by femtosecond laser pulses with fluence above threshold have been demonstrated in Refs. [43, 44]. Since then a lot of effort was put to study kinetics of magnetization [45–50], crystal lattice [48, 49, 51–53] spin current [54] and electronic distribution [55] during photoinduced phase transition (PIPT). The main stages of the PIPT were uncovered, and include sub-picosecond charge redistribution between Fe and Rh ions [55] followed by an 8 ps nucleation of FM phase [47, 48] leading to growth and alignment of FM domains within 50-80 ps depending on experimental parameters [45, 50, 52]. The lattice expansion during PIPT follows time evolution of the FM phase volume fraction

<sup>\*</sup> mogunov@mail.ioffe.ru

[49] with a time constant of 95 ps [51].

The lattice change during the first-order PIPT was used previously to produce tunable high-amplitude bulk longitudinal acoustic pulses in an archetypical first-order phase transition material VO<sub>2</sub> [56]. Several works investigated the bulk longitudinal acoustic pulse generation in FeRh [48, 51, 54] finding that it is generated and leaves the excitation area on a timescale significantly shorter than that of the PIPT-related strain. As a result, the latter provides no noticeable contribution to the amplitude of a longitudinal strain pulse [48]. On the other hand, SAWs propagate much slower than the longitudinal acoustic waves, which poses questions: can lattice transformation during PIPT in FeRh be used to generate pulses of SAWs and can their parameters be tuned by inducing the AFM-FM phase transition by external stimuli such as heating?

In this work we generate SAW pulses directly in FeRh film using femtosecond laser pulses and investigate their tunability by varying external temperature and excitation fluence both below and above corresponding phase transition thresholds. We observe SAWs in FeRh/MgO (001) system via photoelastic effect as well as surface displacement and reveal a nonlinear increase of their amplitudes with increasing laser fluence when  $T < T_{PT}$ . For a fixed above-threshold fluence the generated SAW amplitude increases when the temperature approaches  $T_{PT}$  from below and then drops for  $T > T_{PT}$ . We devise a model attributing these findings to a pronounced contribution to SAW generation from a lattice expansion during PIPT.

## II. EXPERIMENTAL DETAILS

As a sample we use a 60 nm epitaxial single-crystalline Fe<sub>49</sub>Rh<sub>51</sub> film grown on a single-crystalline MgO (001) substrate by molecular beam epitaxy capped with 2 nm gold layer to prevent oxidation (for details on sample growth see [29]). FeRh layer is grown in (001) orientation confirmed by X-Ray diffraction and has low  $3.7 \times 10^{-3}$ compressive in-plane epitaxial strain. Surface roughness is 0.7 nm (see Supplemental Material Sec. I(A) [57]). Epitaxial relations and schematic of the sample are shown on Fig. 1(a). Equilibrium phase transition is characterized by emergence of magnetization above  $T_{PT}$  in external magnetic field  $\mu_0 H = 100$  mT along [110]<sub>FeRh</sub> (in-plane) exceeding the coercive field in FM phase,  $\mu_0H=6$  mT (see Supplemental Material sec. I(C) [57]). We find temperature of AFM-FM transition  $T_{PT}$ =367 K with width of the temperature hysteresis  $\Delta T$ =21 K (Fig. 1(b)). For FeRh films thermal hysteresis of magnetization matches the thermal hysteresis of its lattice parameters [58].

In experiments we excite and detect SAWs optically using a femtosecond pump-probe scanning microscopy where probe pulse reflectivity change is used to detect SAWs via photoelastic effect sensitive to various strain tensor elements including in-plane strain [59]. The

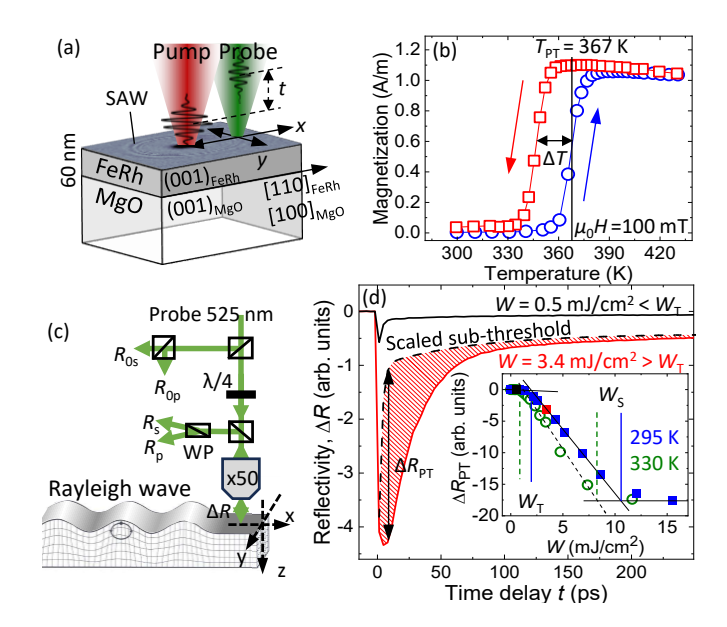


FIG. 1. Scheme of experiment and sample characterization. (a) Scheme of sample and experiment; (b) Thermal hysteresis of magnetization for external in-plane field  $\mu_0H=100$  mT; (c) Sketch of photoelastic SAW detection. WP is a Wollastone prism,  $\lambda/4$  is a quarter-wave plate; (d) Transient reflectivity change  $\Delta R(t)$  for pump fluences 0.5 mJ/cm² (black) and 3.4 mJ/cm² (red) at 295 K. Dotted black curve is the scaled version of solid black one. Shaded area is a phase transition contribution to reflectivity  $\Delta R_{PT}$ . Inset: fluence dependence of maximal  $\Delta R_{PT}$  value used to find threshold and saturation fluences at 295 (blue squares) and 330 K (green circles).

scheme of experiment is shown on Figs 1(a),(c) (see also Supplemental Material Sec. II [57]). Both pump and probe pulses have duration 150 fs and are focused by ×50 micro-objective on the sample surface with normal incidence. Pump pulses have wavelength 680 nm and are linearly polarized, probe pulses have wavelength 525 nm and are circularly polarized. Pump and probe spots on the sample surface are circular with FWHM = 0.9  $\mu$ m and  $0.7 \mu m$ , respectively. The measured laser spots are larger than typical domain [60] and grain [58] sizes for thin FeRh films with no external magnetic field and order of magnitude larger than the typical size of FM phase nucleation sites [60]. The SAWs are generated in FeRh film since MgO substrate is optically transparent, pump penetration depth is 20 nm [61] therefore pump is fully absorbed in the 60 nm-thick film. In experiments we detect intensity of probe pulses reflected from the sample, monitoring separately their p- and s- polarization components. We use balanced detection with a reference beam to enhance signal-to-noise ratio. Time resolution in experiments is <100 fs and spatial resolution is  $0.3 \mu m$ . The sample is mounted on a heater allowing temperature control with 1 K precision for up to 500 K covering the range below and above  $T_{PT}$ =367 K (Fig. 1(b)).

#### III. RESULTS

First, we characterize PIPT in the FeRh film in AFM state at room temperature 295 K and at a temperature close to the phase transition, 330 K (Fig. 1(b)). To do it we measure reflectivity change vs time delay,  $\Delta R/R(t)$ , for a set of pump fluences W. Below threshold fluence  $W_T$ ,  $\Delta R/R(t)$  grows linearly with W. To acquire the PIPT-related reflectivity change the scaled signal for sub-threshold fluence is subtracted from each measured curve - an established procedure for FeRh films [45, 49]. The result is presented on Fig. 1(d) for 295 K. We note that reflectivity for the probe wavelength 525 nm is reduced upon PIPT which is in accordance with spectral changes for temperature-driven AFM-FM transition [61, 62]. The amplitude of PIPT-related reflectivity change vs pump fluence (inset in Fig. 1(d)) is clearly non-linear for both initial sample temperatures. At threshold fluence  $W_T$  the PIPT starts to take place at some nucleation sites, while above saturation fluence  $W_S$  the whole FeRh film undergoes the transition. We evaluate  $W_T = 2 \text{ mJ/cm}^2$ ,  $W_S = 10.6 \text{ mJ/cm}^2$  at  $T_0 = 295 \text{ K}$ and for  $T=330 \text{ K } W_T=1.2 \text{ mJ/cm}^2, W_S=8.3 \text{ mJ/cm}^2$  at  $T_0=330$  K. The obtained values are close to those reported in literature [45, 48]. In the main experiments we detect laser-generated SAWs and explore the PIPT contribution to the acoustic wave generation. To do so we fix the time delay t between pump and probe pulses and scan the probe spot position on the sample surface to obtain 2D maps  $\Delta R_s/R$ . Delay t=3 ns is chosen so that the SAW pulses with characteristic velocities of several km/s have enough time to leave the area excited by a pump pulse which is also transformed into FM phase for  $W > W_T$ . Therefore the SAWs are detected in parts of the sample remaining in the initial state defined by the temperature of the heater. We perform measurements for three initial sample temperatures below, close to, and above  $T_{PT}$  and for a set of pump fluences ranging from below  $W_T$  to above  $W_S$ .

Fig. 2 shows exemplary 2D maps of reflectivity change as well as their cross-sections at y=0 obtained at T=295 K, 330 K and 430 K and pump fluence 14 mJ/cm<sup>2</sup> well above  $W_S$ . On Figs. 2(a)-(c) along with the reflectivity change inside the pump spot (same as Fig. 1(d)) one can see a set of concentric rings. The rings belong to a laser-induced wave propagating away from the excitation spot with a phase velocity  $v=\sim5.5$  km/s estimated from its shape at several time delays (see Supplemental Material Sec. III [57]). Within experimental precision this velocity is the same for AFM and FM initial phase of FeRh, hence the detected wave is not a spin wave since dispersion of the latter changes drastically upon the AFM-FM transformation [63, 64]. For a substrate loaded by a thin metallic film one can expect three acoustic waves traveling along the surface: quasi-Rayleigh wave, Love wave and a surface-skimming longitudinal acoustic (SSLA) wave, with the quasi-Rayleigh wave being the slowest [15, 65]. The closest to the obtained velocity v is the Rayleigh group velocity in MgO (001) plane  $v_R$ =5.5-5.7 km/s [66]. This two factors allow us to ascribe the observed wave to a quasi-Rayleigh SAW in FeRh/MgO (001) system. The small difference between v and  $v_R$  is due to mechanical loading of MgO substrate by FeRh film which is a well-known feature of SAWs in a 'substrate-film' system [65]. Only a weak signature of the SSLA wave packet is present in the data, and no Love wavepacket is observed. Therefore we limit further discussion to quasi-Rayleigh wave and refer to it as 'SAW'.

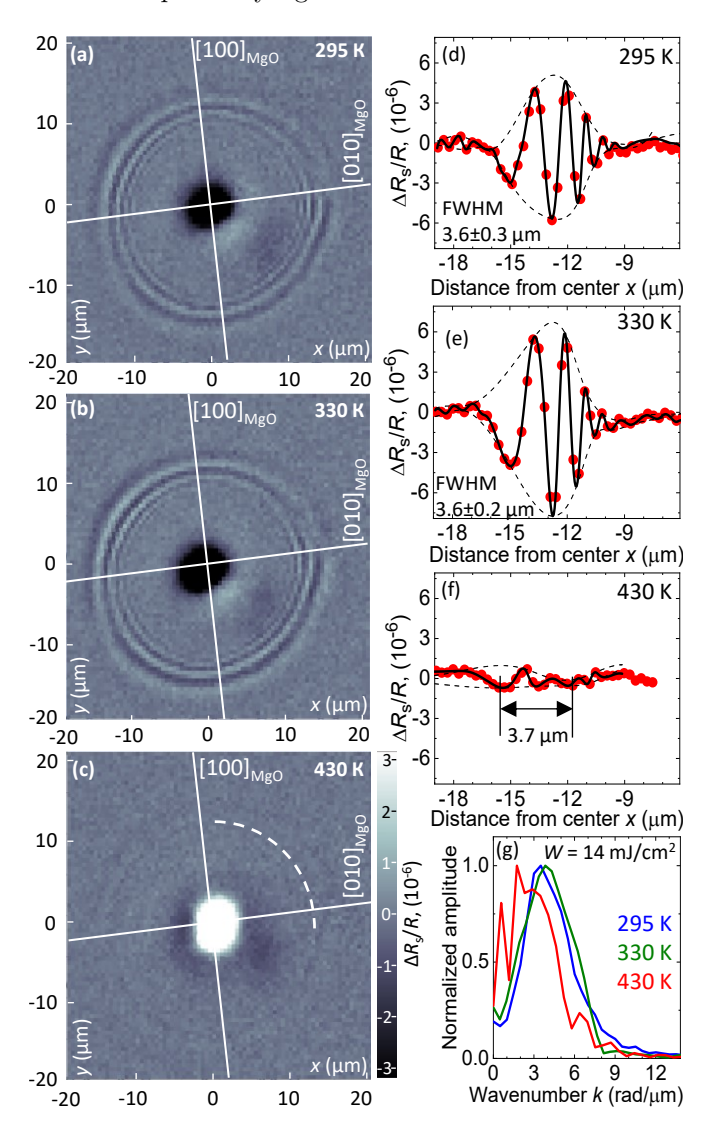


FIG. 2. SAW pulses in FeRh/MgO (001) detected by photoelastic effect below and above phase transition temperature. (a)-(c) 2D spatial maps of  $\Delta R_s/R$  for t=3 ns after excitation for initial sample temperatures (a)  $T_0=295$  K $< T_{PT}$ , (b)  $T_0=330$  K $< T_{PT}$  and (c)  $T_0=430$  K $> T_{PT}$ . Pump fluence is above saturation: W=10 mJ/cm² >  $W_s$ . (d)-(f) 1D scans along x direction for the same set of temperatures as (a)-(c). Dots are experimental data, solid lines are S-spline interpolation, dotted lines are envelops used to determine signal amplitudes; (g) Normalized FFTs of the SAW pulses from (d)-(f).

Figures 2(d)-(f) show 1D scans along x direction re-

vealing the detailed wavepackets' shape. Solid lines show the interpolation of data points and dotted lines show the envelope of interpolated data. The FWHM of envelope at t=3 ns is 3.6  $\mu m$  and is the same for 295 and 330 K. It is not possible to accurately determine FWHM for  $T_0$ =430 K but the estimation based on the signal shape yields similar value 3.7  $\mu$ m. Clear chirping is seen within the wavepacket caused by dispersion of acoustic phonons constituting the SAW pulse as commonly observed for laser-generated SAWs [15, 67–69]. Figure 2(g) shows a fast Fourier transform (FFT) of the pulses from panels (d)-(f), normalized for clarity. The detected SAWs possess relatively large k-vectors reaching 7.5 rad/ $\mu$ m<sup>-1</sup>. The dominant k-vector shifts slightly to lower values for  $T_0$ =430 K for all the used laser fluences although this shift cannot be confidently evaluated due to low signal amplitude at 430 K. The corresponding SAW wavelengths exceed 0.8  $\mu m$  and are considerably larger than the FeRh film thickness 60 nm. Therefore the bulk of acoustic energy travels in the substrate and is described by parameters of the substrate [65]. This also explains the apparent 4-fold symmetry on Figs. 2(a)-(c) which is attributed to (001)-cut MgO substrate.

The main parameter that changes with temperature is the amplitude of observed SAW pulses, diminishing by a factor of 8 for  $T_0$ =430 K. For photoelastic method of SAW detection this signal drop upon changing the equilibrium state of FeRh film can be caused by two factors. First, the decrease of laser-generated strain leads to the lower amplitude in the SAW. Second, the decrease of FeRh photoelastic constants in FM phase leads to smaller detected reflectivity modulation  $\Delta R_s/R$  associated with the SAW. To verify that it is the generated strain that drops above  $T_{PT}$ , we perform an independent scanning pump-probe measurements with a different detection technique – laser Sagnac interferometry (Fig. 3(a)) described in [68, 69]. This technique is mainly sensitive to atomic displacement along the surface normal and is widely used to detect quasi-Rayleigh SAW pulses [15, 67–70]. In this experiment laser spots on the sample are larger, 1  $\mu$ m for 800 nm probe and 1.8  $\mu$ m for 400 nm pump.

Figs. 3(b)-(c) show 2D maps of an interferometric phase difference  $\Delta \varphi$ , proportional to the surface displacement, for AFM  $(T_0=305 \text{ K})$  and FM  $(T_0=430 \text{ K})$  initial state of FeRh film taken 3 ns after pump excitation with above-threshold fluence  $W=13 \text{ mJ/cm}^2$ . All the features of the SAWs revealed by photoelastic detection (Figs. 2(a)-(c)) are present in these scans as well. Most importantly the interferometric signal amplitude in FM FeRh state is  $\sim 4$  times lower than in the AFM FeRh state, in qualitative agreement with photoelastic results (Figs. 2(a)-(c)). Therefore we conclude that the laserinduced SAW amplitude does significantly decrease when generated in FM phase as compared to the initial AFM phase. This suggests that the PIPT occurring only when FeRh is in the AFM state provides a noticeable contribution to the SAW pulse generation.

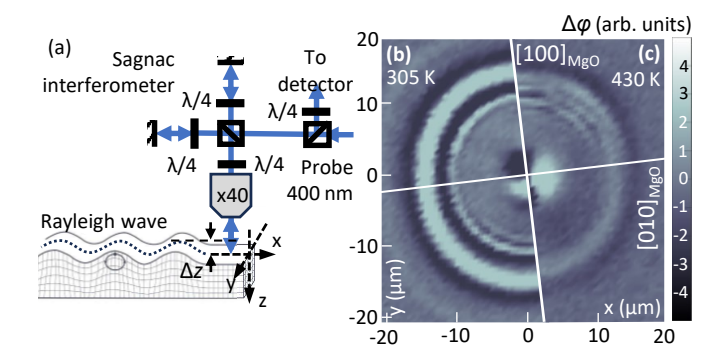


FIG. 3. SAW pulses in FeRh/MgO (001) detected by interferometry below and above AFM-FM transition temperature. (a) Sketch of interferometer [68] used to detect quasi-Rayleigh SAW.  $\lambda/4$  are quater-wave plates; (b)-(c) 2D spatial maps of  $\Delta\varphi$  for  $t{=}3$  ns after excitation with above-threshold fluence  $W{=}13$  mJ/cm² for initial sample temperatures (b)  $T_0305$  K< $T_{PT}$  and (c)  $T_0430$  K> $T_{PT}$ .

### IV. DISCUSSION

When considering materials with 1st order PIPTs excited by femtosecond laser pulses the strain generation process becomes non-trivial as compared to conventional optoacoustic transducers [71–73]. This includes the change of material parameters happening during the onset of picosecond strain as well as direct contribution from lattice transformation during phase transition which can differ from eventual structural change under quasi-equilibrium conditions [56]. The central frequency of the phonons in a SAW pulse, f, is a measure of the timescale of generation process [73]. The value of fcan be estimated from wavevector k, corresponding to the maximal spectral amplitude (Fig. 2(g)), and SAW sound velocity:  $f = kv/2\pi = 3.1$  GHz. Corresponding time period  $\tau$ =320 ps is much longer than the duration of the main stages of PIPT such as 8 ps FM phase emergence [47, 48] and 50 ps FM phase coalescence [45, 52]. Therefore the generation of strain responsible for SAW is regulated by material constants in photoinduced state of FeRh, which is a mix of initial AFM and laser-transformed FM phases, and is governed by heat diffusion [49] as is typically considered for laser-generated SAWs [74, 75]. However the quaterperiod of the SAW  $\tau/4=80$  ps matches well with the 95 ps timescale of lattice transformation during PIPT [51, 52] implying that PIPT plays a role in the SAW generation.

In our experiments we detect the SAW pulse that has already left the region of generation contrary to X-ray diffraction experiments performed within the excitation area [48, 51, 52]. The SAW pulse propagating along x has in-plane  $\varepsilon_{xx}^{SAW}$  and out-of-plane  $\varepsilon_{zz}^{SAW}$  strain components which we detect within probe penetration depth of 24 nm in AFM phase and 29 nm in FM phase [61]. Therefore the detected signal comes only from thin FeRh film which allows us to link the strain components using boundary conditions on a free surface:  $\varepsilon_{zz}^{SAW}/\varepsilon_{xx}^{SAW} = -\nu/(1-\varepsilon_{xx}^{SAW})$ 

 $\nu)$  [76] where  $\nu$  is Poisson ratio. Using the values of  $\nu$  from [77] we get  $\varepsilon_{xx,AFM}^{SAW}=2.1\varepsilon_{zz,AFM}^{SAW}$  in AFM phase and  $\varepsilon_{xx,FM}^{SAW}=2.9\varepsilon_{zz,FM}^{SAW}$  in FM phase. This lets us to consider only in-plane SAW strain component.

To distinguish between various contributions to the generated strain the dependencies of SAW amplitude on absorbed energy density J are studied at three initial sample temperatures (symbols on Fig. 4). For our data we calculate the values J from the incident fluence Wtaking into account the full film thickness 60 nm rather than pump penetration depth 20 nm [61] since the SAW generation occurs slower than heat redistribution of the deposited laser energy over the film thickness with a characteristic time of 50 ps [48, 49, 78]. Two main conclusions can be drawn directly from the graphs. (i) For a fixed temperature  $T < T_{PT}$ , the dependence of SAW amplitude on absorbed energy density shows nonlinear behavior featuring the temperature-dependent threshold at  $J_T$ and saturation at  $J_S$ , similar to PIPT (inset in Fig. 1(d)). This behavior is analogous to previous reports on longitudinal acoustic wave generated during 1st order PIPT [56]. At  $T > T_{PT}$ , the generated SAW exhibits linear dependence on J. (ii) For a fixed above-threshold energy density  $J > J_T$ , the SAW amplitude increases with temperature until  $T_{PT}$  is reached and drops drastically afterwards. This behavior is similar to a standalone report on SAW generation by nanosecond pulsed laser in iron near Curie temperature [79] which was explained by strong anomaly of thermal expansion coefficient due to laser-heating induced dissociation of magnetic order causing elastic disbalance (see also [80]). Similar disbalance can be caused by lattice rearrangement during PIPT and can contribute to strain generation only below  $T_{PT}$ for  $J > J_T$ .

Below we describe the mechanisms of laser generated strain in FeRh and how we include them in our model. Typically when analyzing laser generation of SAWs in metals, only thermoelastic effect is considered. The strain  $\varepsilon_{th}$  is evaluated by solving together heat diffusion and thermoelastic equations utilizing linear thermal expansion coefficient  $\alpha$  [74, 75]. For a thin film the strain generated through thermoelastic effect in z direction can be calculated in a simplified form  $\varepsilon_{th}(J) = \int_{T_0}^{T(J)} \alpha(T') dT'$  [56, 71] where T(J) is a laser-induced temperature. The value of  $\alpha$  of FeRh alloy was found to drop above  $T_{PT}$  and to raise back above Curie temperature  $T_c = 680 \ K$  [38].

The second mechanism is a strain  $\varepsilon_{PT}$  imposed by lattice transformation during PIPT [56]. We assume that PIPT-associated strain does not depend on initial sample temperature if it is lower than  $T_{PT}$ . The strain evolution upon PIPT in thin FeRh films on MgO (001) was studied extensively by X-ray diffraction [48, 51, 52, 81] and the lattice change in z direction was measured to be  $\varepsilon_{PT}=6\times 10^{-3}$  for relatively thick FeRh film such as ours [48]. We estimate the expected in-plane SAW strain due to a  $\varepsilon_{PT}$  to be  $\varepsilon_{PT,xx}^{SAW}=4\times 10^{-5}$  (see Supplemental

Material, sec. IV [57]) by utilizing a model of an infinite stripe applying time-dependent pressure on a substrate [82, 83]. This estimation allow us to get the conversion coefficient between laser-generated strain along z and inplane component of SAW  $s = \varepsilon_{xx}^{SAW}/\varepsilon \approx 0.07$ . Finally, magnetostriction [84, 85], spin-stress [86–88]

Finally, magnetostriction [84, 85], spin-stress [86–88] and electron gas pressure [72] can contribute to the strain generation. As we apply no magnetic field, the magnetic mechanisms are included into  $\alpha(T)$  while the latter we expect to have no significant contribution because in FeRh electron-phonon interaction is strong and electrons thermalize within several hundreds of femtoseconds [89]. Additionally, no piezoelectric mechanism [72] is expected because both FeRh and MgO have centrosymmetric crystal lattices.

Due to the first-order nature of the AFM-FM transition the two phases of FeRh can coexist. When considering the lattice change contribution one have to account for distribution of local  $T_{PT}^*$  values of individual nucleation sites [60]. In calculations we assume that each nucleation cite possesses a sharp and full transition at individual  $J_{PT}^*$ . This gives a meaning to values  $J_T$  and  $J_S$  as boundaries of distribution of  $J_{PT}^*$  which we considered to be Gaussian centered at  $J_m = (J_T + J_S)/2$  with dispersion  $\sigma = (J_S - J_T)/6$ . The expression used to calculate laser-induced strain  $\varepsilon$  is:

$$\varepsilon(J) = \sum_{J_T < J_{PT}^* < J_S} \left[ \frac{\exp\left[ (J_{PT}^* - J_m)^2 / 2\sigma^2 \right]}{\sqrt{2\pi}\sigma} \times \left( \varepsilon_{th}(J, J_{PT}^*) + \theta(J - J_{PT}^* - J_L) \varepsilon_{PT} \right) \right]$$
(1)

where  $\theta$  is Heaviside function.

To calculate thermoelastic contribution from an individual nucleation site  $\varepsilon_{th}(J,J_{PT}^*)$  we first evaluate laser-induced temperature T via absorbed energy J and specific heat C:  $J-\theta(J-J_{PT}^*-J_L)J_L=\int_{T_0}^T C(T',T_{PT}^*)dT'$ , where  $J_L$ =5.32 J/m³ is latent heat [90] and  $T_{PT}^*$  is calculated using the expression above with  $J=J_{PT}^*$ . In the range between  $J_{PT}^*$  and  $J_{PT}^*+J_L$  the temperature is constant  $T=T_{PT}^*$  as the phase transition is of the 1st order. The thermoelastic contribution  $\varepsilon_{th}$  is then calculated by integrating linear thermal expansion coefficient between initial temperature and T. Both  $C(T,T_{PT}^*)$  and  $\alpha(T,T_{PT}^*)$  are linear approximations of specific heat [90] and linear thermal expansion [38], respectively, above 295 K with discontinuities at  $T_{PT}^*$  and  $T_c$  (see Supplemental Material sec. V [57]).

In calculations the threshold value  $J_T$  is defined by FM phase nucleation occurring within the penetration depth of the laser pulse. Saturation  $J_S$  is defined by slower thermal transformation across the whole depth of the FeRh film [49]. This also means that  $J_S/J_T \neq W_S/W_T$  since  $W_T$  and  $W_S$  are extracted from the change of optical properties within the probe penetration depth and possess no information about deeper regions of the FeRh film [48] while  $J_T$  and  $J_S$  are associated with the SAW

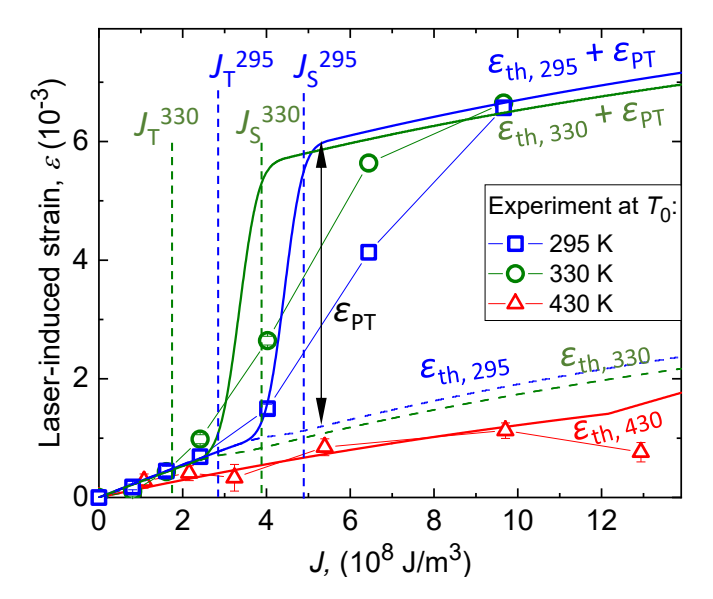


FIG. 4. Laser-induced strain generation during PIPT in FeRh. Calculation results (lines) and experimental data (symbols) for initial sample temperatures  $T_0$ =295 K (blue, squares), 330 K (green, circles) and 430 K (red, triangles). The calculations performed in accordance with Eq. (1). The dashed lines show calculation result with  $\varepsilon_{PT}=0$ ;

generation. Such definition of  $J_T$  and  $J_S$  allows better agreement between experimental and calculation results.

The main result is shown on Fig. 4 where we plot calculation results (lines) along with the data (dots) for three initial temperatures. The experimental SAW amplitudes are vertically scaled so that they coincide with the calculations in the region  $J < J_T$ . This yields different scaling factors  $p = (\Delta R_s/R)/(\varepsilon s)$  for different initial phases:  $p_{AFM} = 0.037$  and  $p_{FM} = 0.02$  where we use the estimated value  $s \approx 0.07$ . The scaling factors account for the possible difference in effective photoelastic constant as well as the change of complex refractive index [91] and attenuation of the SAW amplitude upon propagation for t=3 ns. Note that the relation  $p_{\text{AFM}}/p_{\text{FM}} \approx 2$ accounts for the difference in signal amplitude drop at 430 K between photoelastic (8 times, Figs. 2(d) and (f)) and interferometric (4 times, Figs 3(b) and (c)) measurements.

The calculations are based on thermodynamic parameters of FeRh meaning that they assume thermalization of the excited sample volume. The calculation describes qualitatively the main observed features of  $T_0$ - and J-dependencies as well as captures general shape of the  $\varepsilon(J,T_0)$  curves. The value of  $\varepsilon_{PT}$  in our calculations is  $4.8\times 10^{-3}$  which is close to the lattice change in z direction in FeRh/MgO films  $6\times 10^{-3}$  [48]. With our calculations we uncovered the reason for large SAW amplitude in AFM phase of FeRh: the large contribution from PIPT enhances the SAW amplitude in AFM phase by a factor of 5, which can be clearly seen in Fig. 4 by comparing solid and dashed lines. Therefore the laser-generated SAW amplitude in FeRh is primar-

ily defined by the AFM-FM phase transition contribution which makes possible the tuning of SAW by controlling the phase of FeRh. Finally, the total in-plane strain amplitude of laser-generated SAWs in FeRh reaching  $\varepsilon s = 4.4 \times 10^{-4}$  which is high enough to show acoustic nonlinearities upon propagation in MgO [92].

#### V. CONCLUSIONS

To conclude, we experimentally studied optically generated SAWs in FeRh/MgO system. To date the reports on SAWs in FeRh are scarce with only two recent works [93, 94] in which SAWs were generated elsewhere by interdigitated transducers and injected in FeRh. In the present work we generated optically quasi-Rayleigh surface acoustic wave pulses with central frequency 3.1 GHz during photoinduced AFM-FM phase transition in a 60 nm thick Fe<sub>49</sub>Rh<sub>51</sub> film on MgO (001) substrate both below and above the AFM-FM transition temperature and for pump laser fluences ranging from sub-threshold to above-saturation level of PIPT excitation. We detected the SAWs optically via photoelastic effect and interferometry. The SAW amplitude for above-threshold fluences rises with temperature below  $T_{PT}$  and decreases dramatically above  $T_{PT}$ . For AFM initial phase, the SAW amplitude grows nonlinearly with increasing pump fluence. This behavior is attributed to the large contribution of the FeRh phase transition to the SAW generation process which is present only for AFM initial phase and above-threshold pump fluences and is responsible for the most of laser-generated strain above threshold. A model based on thermodynamic parameters of FeRh was able to successfully describe the main features of observed SAW amplitude dependencies on  $T_0$  and J. This proves that 90 ps lattice transformation in feRh contributes effectively to the SAW generation while non-equilibrium PIPT dynamics does not.

Based on our results one can envision an optically-activated on-chip ultrafast SAW emitter in integrated magnetoacoustic device controlled by switching between magnetic state, AFM or FM, of FeRh. Since FeRh was proposed earlier as a memory cell [33, 34], that stores information in AFM state while writing is realized in FM state, such a SAW emitter would be automatically switched off when the data is being rewritten. Utilization of such a controlled acoustical cross-talk can also be used in a neuromorphic device where phase-changing FeRh elements would be neurons, their AFM-FM phase ratio being a weight [22], and the SAW acting as a synaptic link which in turn can affect the state of the other FeRh neuron [94].

## ACKNOWLEDGMENTS

Authors thank P. I. Gerevenkov and Ia. A. Filatov for the help with experiments and fruitful discussions. The research was supported by Russian Science Foundation grant No. 24-72-00111. The interferometry experiments were supported by Russian Science Foundation Grant No. 23-12-00251.

- V. Baltz, A. Manchon, M. Tsoi, T. Moriyama, T. Ono, and Y. Tserkovnyak, Antiferromagnetic spintronics, Rev. Mod. Phys. 90, 015005 (2018).
- [2] T. Jungwirth, X. Marti, P. Wadley, and J. Wunderlich, Antiferromagnetic spintronics, Nature Nanotechnology 11, 231–241 (2016).
- [3] J. Han, R. Cheng, L. Liu, H. Ohno, and S. Fukami, Coherent antiferromagnetic spintronics, Nature Materials 22, 684–695 (2023).
- [4] A. A. Bukharaev, A. K. Zvezdin, A. P. Pyatakov, and Y. K. Fetisov, Straintronics: a new trend in micro- and nanoelectronics and material science, Phys. Usp. 61, 1175 (2018).
- [5] M. Weiler, L. Dreher, C. Heeg, H. Huebl, R. Gross, M. S. Brandt, and S. T. B. Goennenwein, Elastically driven ferromagnetic resonance in nickel thin films, Phys. Rev. Lett. 106, 117601 (2011).
- [6] C. Berk, M. Jaris, W. Yang, S. Dhuey, S. Cabrini, and H. Schmidt, Strongly coupled magnon-phonon dynamics in a single nanomagnet, Nature Communications 10, 2652 (2019).
- [7] A. V. Scherbakov, A. S. Salasyuk, A. V. Akimov, X. Liu, M. Bombeck, C. Brüggemann, D. R. Yakovlev, V. F. Sapega, J. K. Furdyna, and M. Bayer, Coherent magnetization precession in ferromagnetic (Ga,Mn)As induced by picosecond acoustic pulses, Phys. Rev. Lett. 105, 117204 (2010).
- [8] V. S. Vlasov, A. V. Golov, L. N. Kotov, V. I. Shcheglov, A. M. Lomonosov, and V. V. Temnov, The modern problems of ultrafast magnetoacoustics (review), Acoustical Physics 68, 18–47 (2022).
- [9] E. Rongione, O. Gueckstock, M. Mattern, O. Gomonay, H. Meer, C. Schmitt, R. Ramos, T. Kikkawa, M. Mičica, E. Saitoh, J. Sinova, H. Jaffrès, J. Mangeney, S. T. B. Goennenwein, S. Geprägs, T. Kampfrath, M. Kläui, M. Bargheer, T. S. Seifert, S. Dhillon, and R. Lebrun, Emission of coherent THz magnons in an antiferromagnetic insulator triggered by ultrafast spin-phonon interactions, Nature Communications 14, 1818 (2023).
- [10] W.-G. Yang and H. Schmidt, Acoustic control of magnetism toward energy-efficient applications, Applied Physics Reviews 8, 021304 (2021).
- [11] Y. Li, C. Zhao, W. Zhang, A. Hoffmann, and V. Novosad, Advances in coherent coupling between magnons and acoustic phonons, APL Materials 9, 060902 (2021).
- [12] N. K. P. Babu, A. Trzaskowska, P. Graczyk, G. Centała, S. Mieszczak, H. Głowiński, M. Zdunek, S. Mielcarek, and J. W. Kłos, The interaction between surface acoustic waves and spin waves: The role of anisotropy and spatial profiles of the modes, Nano Letters 21, 946 (2021).
- [13] P. I. Gerevenkov, I. A. Mogunov, I. A. Filatov, N. S. Gusev, M. V. Sapozhnikov, N. E. Khokhlov, and A. M. Kalashnikova, Three regimes of a picosecond magnetoacoustics in ferromagnetic structures, arXiv:2505.09579.
- [14] D. D. Yaremkevich, A. V. Scherbakov, S. M. Kukhtaruk, T. L. Linnik, N. E. Khokhlov, F. Godejohann, O. A. Dyatlova, A. Nadzeyka, D. P. Pattnaik, M. Wang, S. Roy,

- R. P. Campion, A. W. Rushforth, V. E. Gusev, A. V. Akimov, and M. Bayer, Protected long-distance guiding of hypersound underneath a nanocorrugated surface, ACS Nano 15, 4802 (2021).
- [15] Y. Sugawara, O. B. Wright, O. Matsuda, M. Takigahira, Y. Tanaka, S. Tamura, and V. E. Gusev, Watching ripples on crystals, Phys. Rev. Lett. 88, 185504 (2002).
- [16] M. van Kampen, C. Jozsa, J. T. Kohlhepp, P. LeClair, L. Lagae, W. J. M. de Jonge, and B. Koopmans, Alloptical probe of coherent spin waves, Phys. Rev. Lett. 88, 227201 (2002).
- [17] A. Papp, W. Porod, and G. Csaba, Nanoscale neural network using non-linear spin-wave interference, Nature Communications 12, 6422 (2021).
- [18] D. D. Yaremkevich, A. V. Scherbakov, L. De Clerk, S. M. Kukhtaruk, A. Nadzeyka, R. Campion, A. W. Rushforth, S. Savel'ev, A. G. Balanov, and M. Bayer, On-chip phonon-magnon reservoir for neuromorphic computing, Nature Communications 14, 8296 (2023).
- [19] M. Kounalakis, S. Viola Kusminskiy, and Y. M. Blanter, Engineering entangled coherent states of magnons and phonons via a transmon qubit, Phys. Rev. B 108, 224416 (2023).
- [20] S. J. Whiteley, G. Wolfowicz, C. P. Anderson, A. Bourassa, H. Ma, M. Ye, G. Koolstra, K. J. Satzinger, M. V. Holt, F. J. Heremans, A. N. Cleland, D. I. Schuster, G. Galli, and D. D. Awschalom, Spin-phonon interactions in silicon carbide addressed by gaussian acoustics, Nature Physics 15, 490–495 (2019).
- [21] T. W. Hughes, I. A. D. Williamson, M. Minkov, and S. Fan, Wave physics as an analog recurrent neural network, Science Advances 5, easy6946 (2019).
- [22] D. Kuzum, R. G. D. Jeyasingh, B. Lee, and H.-S. P. Wong, Nanoelectronic programmable synapses based on phase change materials for brain-inspired computing, Nano Letters 12, 2179–2186 (2011).
- [23] A. I. Zakharov, A. M. Kadomtseva, R. Z. Levitin, and E. G. Ponyatovskii, Magnetic and magnetoelastic properties of a metamagnetic iron-rhodium alloy, Sov. Phys. JETP 19, 1348 (1964).
- [24] G. Shirane, C. W. Chen, P. A. Flinn, and R. Nathans, Hyperfine fields and magnetic moments in the Fe–Rh system, Journal of Applied Physics 34, 1044 (1963).
- [25] L. J. Swartzendruber, The Fe-Rh (iron-rhodium) system, Bulletin of Alloy Phase Diagrams 5, 456–462 (1984).
- [26] V. I. Zverev, R. R. Gimaev, T. Miyanaga, A. A. Vaulin, A. F. Gubkin, B. B. Kovalev, A. M. dos Santos, E. Lovell, L. F. Cohen, and N. A. Zarkevich, Peculiarities of the phase transformation dynamics in bulk FeRh based alloys from magnetic and structural measurements, Journal of Magnetism and Magnetic Materials 522, 167560 (2021).
- [27] J. Cao, N. T. Nam, S. Inoue, H. Y. Y. Ko, N. N. Phuoc, and T. Suzuki, Magnetization behaviors for FeRh single crystal thin films, Journal of Applied Physics 103, 07F501 (2008).
- [28] S. Maat, J.-U. Thiele, and E. E. Fullerton, Temperature and field hysteresis of the antiferromagnetic-to-

- ferromagnetic phase transition in epitaxial FeRh films, Phys. Rev. B **72**, 214432 (2005).
- [29] A. S. Komlev, D. Y. Karpenkov, D. A. Kiselev, T. S. Ilina, A. Chirkova, R. R. Gimaev, T. Usami, T. Taniyama, V. I. Zverev, and N. S. Perov, Ferromagnetic phase nucleation and its growth evolution in FeRh thin films, Journal of Alloys and Compounds 874, 159924 (2021).
- [30] I. Suzuki, T. Koike, M. Itoh, T. Taniyama, and T. Sato, Stability of ferromagnetic state of epitaxially grown ordered FeRh thin films, Journal of Applied Physics 105, 07E501 (2009).
- [31] Z. Feng, H. Yan, and Z. Liu, Electric-field control of magnetic order: From FeRh to topological antiferromagnetic spintronics, Advanced Electronic Materials 5, 1800466 (2019).
- [32] I. Fina and J. Fontcuberta, Strain and voltage control of magnetic and electric properties of FeRh films, Journal of Physics D: Applied Physics 53, 023002 (2019).
- [33] X. Marti, I. Fina, C. Frontera, J. Liu, P. Wadley, Q. He, R. J. Paull, J. D. Clarkson, J. Kudrnovský, I. Turek, J. Kuneš, D. Yi, J.-H. Chu, C. T. Nelson, L. You, E. Arenholz, S. Salahuddin, J. Fontcuberta, T. Jungwirth, and R. Ramesh, Room-temperature antiferromagnetic memory resistor, Nature Materials 13, 367–374 (2014).
- [34] T. Moriyama, N. Matsuzaki, K.-J. Kim, I. Suzuki, T. Taniyama, and T. Ono, Sequential write-read operations in FeRh antiferromagnetic memory, Applied Physics Letters 107, 122403 (2015).
- [35] J.-U. Thiele, S. Maat, and E. E. Fullerton, FeRh/FePt exchange spring films for thermally assisted magnetic recording media, Applied Physics Letters 82, 2859–2861 (2003).
- [36] M. Wolloch, M. E. Gruner, W. Keune, P. Mohn, J. Redinger, F. Hofer, D. Suess, R. Podloucky, J. Landers, S. Salamon, F. Scheibel, D. Spoddig, R. Witte, B. Roldan Cuenya, O. Gutfleisch, M. Y. Hu, J. Zhao, T. Toellner, E. E. Alp, M. Siewert, P. Entel, R. Pentcheva, and H. Wende, Impact of lattice dynamics on the phase stability of metamagnetic FeRh: Bulk and thin films, Phys. Rev. B 94, 174435 (2016).
- [37] L. H. Lewis, C. H. Marrows, and S. Langridge, Coupled magnetic, structural, and electronic phase transitions in FeRh, Journal of Physics D: Applied Physics 49, 323002 (2016).
- [38] M. R. Ibarra and P. A. Algarabel, Giant volume magnetostriction in the FeRh alloy, Phys. Rev. B 50, 4196 (1994).
- [39] J. Ricodeau and D. Melville, High field magnetostriction in a meta-magnetic FeRh alloy, Journal de Physique 35, 149–152 (1974).
- [40] V. I. Zverev, A. M. Saletsky, R. R. Gimaev, A. M. Tishin, T. Miyanaga, and J. B. Staunton, Influence of structural defects on the magnetocaloric effect in the vicinity of the first order magnetic transition in Fe50.4Rh49.6, Applied Physics Letters 108, 192405 (2016).
- [41] N. A. Zarkevich and V. I. Zverev, Viable materials with a giant magnetocaloric effect, Crystals 10, 815 (2020).
- [42] P. A. Algarabel, M. R. Ibarra, C. Marquina, A. del Moral, J. Galibert, M. Iqbal, and S. Askenazy, Giant roomtemperature magnetoresistance in the FeRh alloy, Applied Physics Letters 66, 3061 (1995).
- [43] G. Ju, J. Hohlfeld, B. Bergman, R. J. M. van de Veer-

- donk, O. N. Mryasov, J.-Y. Kim, X. Wu, D. Weller, and B. Koopmans, Ultrafast generation of ferromagnetic order via a laser-induced phase transformation in FeRh thin films, Physical Review Letters **93**, 197403 (2004).
- [44] J.-U. Thiele, M. Buess, and C. H. Back, Spin dynamics of the antiferromagnetic-to-ferromagnetic phase transition in FeRh on a sub-picosecond time scale, Applied Physics Letters 85, 2857 (2004).
- [45] B. Bergman, G. Ju, J. Hohlfeld, R. J. M. van de Veerdonk, J.-Y. Kim, X. Wu, D. Weller, and B. Koopmans, Identifying growth mechanisms for laser-induced magnetization in FeRh, Phys. Rev. B 73, 060407 (2006).
- [46] I. A. Dolgikh, T. G. H. Blank, A. G. Buzdakov, G. Li, K. H. Prabhakara, S. K. K. Patel, R. Medapalli, E. E. Fullerton, O. V. Koplak, J. H. Mentink, K. A. Zvezdin, A. K. Zvezdin, P. C. M. Christianen, and A. V. Kimel, Ultrafast emergence of ferromagnetism in antiferromagnetic FeRh in high magnetic fields, npj Spintronics 3, 5 (2025).
- [47] G. Li, R. Medapalli, J. H. Mentink, R. V. Mikhaylovskiy, T. G. H. Blank, S. K. K. Patel, A. K. Zvezdin, T. Rasing, E. E. Fullerton, and A. V. Kimel, Ultrafast kinetics of the antiferromagnetic-ferromagnetic phase transition in FeRh, Nature Communications 13, 2998 (2022).
- [48] M. Mattern, J. Jarecki, J. A. Arregi, V. Uhlíř, M. Rössle, and M. Bargheer, Speed limits of the laser-induced phase transition in FeRh, APL Materials 12, 051124 (2024).
- [49] M. Mattern, S. P. Zeuschner, M. Rössle, J. A. Arregi, V. Uhlíř, and M. Bargheer, Non-thermal electrons open the non-equilibrium pathway of the phase transition in FeRh, Communications Physics 8, 140 (2025).
- [50] I. Radu, C. Stamm, N. Pontius, T. Kachel, P. Ramm, J.-U. Thiele, H. A. Dürr, and C. H. Back, Laserinduced generation and quenching of magnetization on FeRh studied with time-resolved X-ray magnetic circular dichroism, Phys. Rev. B 81, 104415 (2010).
- [51] F. Quirin, M. Vattilana, U. Shymanovich, A.-E. El-Kamhawy, A. Tarasevitch, J. Hohlfeld, D. von der Linde, and K. Sokolowski-Tinten, Structural dynamics in FeRh during a laser-induced metamagnetic phase transition, Phys. Rev. B 85, 020103 (2012).
- [52] S. O. Mariager, F. Pressacco, G. Ingold, A. Caviezel, E. Möhr-Vorobeva, P. Beaud, S. L. Johnson, C. J. Milne, E. Mancini, S. Moyerman, E. E. Fullerton, R. Feidenhans'l, C. H. Back, and C. Quitmann, Structural and magnetic dynamics of a laser induced phase transition in FeRh, Phys. Rev. Lett. 108, 087201 (2012).
- [53] T. D. Frazer, Y. Zhu, Z. Cai, D. A. Walko, C. Adamo, D. G. Schlom, E. E. Fullerton, P. G. Evans, S. O. Hruszkewycz, Y. Cao, and H. Wen, Optical transient grating pumped X-ray diffraction microscopy for studying mesoscale structural dynamics, Scientific Reports 11, 19322 (2021).
- [54] K. Kang, H. Omura, D. Yesudas, O. Lee, K.-J. Lee, H.-W. Lee, T. Taniyama, and G.-M. Choi, Spin current driven by ultrafast magnetization of FeRh, Nature Communications 14, 3619 (2023).
- [55] F. Pressacco, D. Sangalli, V. Uhlíř, D. Kutnyakhov, J. A. Arregi, S. Y. Agustsson, G. Brenner, H. Redlin, M. Heber, D. Vasilyev, J. Demsar, G. Schönhense, M. Gatti, A. Marini, W. Wurth, and F. Sirotti, Subpicosecond metamagnetic phase transition in FeRh driven by non-equilibrium electron dynamics, Nature Communications 12, 5088 (2021).

- [56] I. A. Mogunov, S. Lysenko, A. E. Fedianin, F. E. Fernández, A. Rúa, A. J. Kent, A. V. Akimov, and A. M. Kalashnikova, Large non-thermal contribution to picosecond strain pulse generation using the photo-induced phase transition in VO<sub>2</sub>, Nature Communications 11, 1690 (2020).
- [57] See Supplemental Material at https://google.com, For details on film characterisation, experimental setups and calculations.
- [58] J. A. Arregi, O. c. v. Caha, and V. c. v. Uhlíř, Evolution of strain across the magnetostructural phase transition in epitaxial FeRh films on different substrates, Phys. Rev. B 101, 174413 (2020).
- [59] T. Saito, O. Matsuda, M. Tomoda, and O. B. Wright, Imaging gigahertz surface acoustic waves through the photoelastic effect, J. Opt. Soc. Am. B 27, 2632 (2010).
- [60] R. C. Temple, T. P. Almeida, J. R. Massey, K. Fallon, R. Lamb, S. A. Morley, F. Maccherozzi, S. S. Dhesi, D. McGrouther, S. McVitie, T. A. Moore, and C. H. Marrows, Antiferromagnetic-ferromagnetic phase domain development in nanopatterned FeRh islands, Phys. Rev. Mater. 2, 104406 (2018).
- [61] V. Saidl, M. Brajer, L. Horák, H. Reichlová, K. Výborný, M. Veis, T. Janda, F. Trojánek, M. Maryško, I. Fina, X. Marti, T. Jungwirth, and P. Němec, Investigation of magneto-structural phase transition in FeRh by reflectivity and transmittance measurements in visible and near-infrared spectral region, New Journal of Physics 18, 083017 (2016).
- [62] S. P. Bennett, M. Currie, O. M. J. van 't Erve, and I. I. Mazin, Spectral reflectivity crossover at the metamagnetic transition in FeRh thin films, Optical Materials Express 9, 2870 (2019).
- [63] A. Castets, D. Tochetti, and B. Hennion, Spin wave spectrum of iron-rhodium alloy in antiferromagnetic and ferromagnetic phases, Physica B+C 86-88, 353 (1977).
- [64] L. M. Sandratskii and P. Buczek, Lifetimes and chirality of spin waves in antiferromagnetic and ferromagnetic FeRh from the perspective of time-dependent density functional theory, Phys. Rev. B 85, 020406 (2012).
- [65] G. Farnell and E. Adler, 2 elastic wave propagation in thin layers, in *Physical Acoustics*, Vol. 9, edited by W. P. Mason and R. Thurston (Academic Press, 1972) pp. 35– 127.
- [66] Y.-C. Lee, J. Kim, and J. Achenbach, Acoustic microscopy measurement of elastic constants and mass density, IEEE Transactions on Ultrasonics, Ferroelectrics, and Frequency Control 42, 253 (1995).
- [67] A. A. Kolomenskii, V. A. Lioubimov, S. N. Jerebtsov, and H. A. Schuessler, Nonlinear surface acoustic wave pulses in solids: Laser excitation, propagation, interactions (invited), Review of Scientific Instruments 74, 448–452 (2003).
- [68] A. Y. Klokov, A. I. Sharkov, V. G. Ralchenko, and V. S. Sedov, Propagation of laser-induced hypersound waves in polycrystalline diamond with submicron crystallites, Journal of Russian Laser Research 42, 580–585 (2021).
- [69] T. Tachizaki, T. Muroya, O. Matsuda, Y. Sugawara, D. H. Hurley, and O. B. Wright, Scanning ultrafast Sagnac interferometry for imaging two-dimensional surface wave propagation, Review of Scientific Instruments 77, 043713 (2006).
- [70] A. Abbas, Y. Guillet, J.-M. Rampnoux, P. Rigail, E. Mottay, B. Audoin, and S. Dilhaire, Picosecond time

- resolved opto-acoustic imaging with 48 MHz frequency resolution, Optics Express 22, 7831 (2014).
- [71] C. Thomsen, H. T. Grahn, H. J. Maris, and J. Tauc, Surface generation and detection of phonons by picosecond light pulses, Phys. Rev. B 34, 4129 (1986).
- [72] P. Ruello and V. E. Gusev, Physical mechanisms of coherent acoustic phonons generation by ultrafast laser action, Ultrasonics 56, 21 (2015).
- [73] O. Matsuda, M. C. Larciprete, R. Li Voti, and O. B. Wright, Fundamentals of picosecond laser ultrasonics, Ultrasonics 56, 3 (2015).
- [74] B. Xu, Z. Shen, X. Ni, J. Lu, and Y. Wang, Finite element model of laser-generated surface acoustic waves in coating-substrate system, Journal of Applied Physics 95, 2109 (2004).
- [75] M. V. Shugaev and L. V. Zhigilei, Thermoelastic modeling of laser-induced generation of strong surface acoustic waves, Journal of Applied Physics 130, 185108 (2021).
- [76] C. Liu, W. Xu, M. Liu, and L. Zhang, Effect of strain path on roughness evolution of free surface during plastic deformation, International Journal of Mechanical Sciences 173, 105475 (2020).
- [77] D. W. Cooke, F. Hellman, C. Baldasseroni, C. Bordel, S. Moyerman, and E. E. Fullerton, Thermodynamic measurements of Fe-Rh alloys, Phys. Rev. Lett. 109, 255901 (2012).
- [78] M. Mattern, J.-E. Pudell, J. A. Arregi, J. Zlámal, R. Kalousek, V. Uhlíř, M. Rössle, and M. Bargheer, Accelerating the laser-induced phase transition in nanostructured FeRh via plasmonic absorption, Advanced Functional Materials 34, 2313014 (2024).
- [79] G. Budenkov, S. Gurevitch, A. Kaunov, and A. Maskaev, Excitation of ultrasound in iron by phase transition under the action of laser pulses, Akusticheskij Zhurnal 29, 561 (1983), [in Russian].
- [80] S. Y. Gurevich and A. A. Shulginov, To the theory of laser generation of elastic waves in ferromagnetic metals at the temperature of magnetic phase transition, Vestnik Yuzhno-Ural'skogo Gosudarstvennogo Universiteta. Seriya "Matematika. Mekhanika. Fizika" 13, 69 (2021), [in Russian].
- [81] M. Grimes, H. Ueda, D. Ozerov, F. Pressacco, S. Parchenko, A. Apseros, M. Scholz, Y. Kubota, T. Togashi, Y. Tanaka, L. Heyderman, T. Thomson, and V. Scagnoli, Determination of sub-ps lattice dynamics in FeRh thin films, Scientific Reports 12, 8584 (2022).
- [82] I. Viktorov, Rayleigh and Lamb Waves: Physical Theory and Applications, Ultrasonic Technology (Springer US, 2013).
- [83] I. Viktorov, Study of Rayleigh wave excitation, Akusticheskij Zhurnal 7, 295 (1961), [in Russian].
- [84] T. Pezeril, [invited] laser generation and detection of ultrafast shear acoustic waves in solids and liquids, Optics & Laser Technology 83, 177 (2016).
- [85] S. P. Zeuschner, T. Parpiiev, T. Pezeril, A. Hillion, K. Dumesnil, A. Anane, J. Pudell, L. Willig, M. Rössle, M. Herzog, A. von Reppert, and M. Bargheer, Tracking picosecond strain pulses in heterostructures that exhibit giant magnetostriction, Structural Dynamics 6, 024302 (2019).
- [86] J. Pudell, A. von Reppert, D. Schick, F. Zamponi, M. Rössle, M. Herzog, H. Zabel, and M. Bargheer, Ultrafast negative thermal expansion driven by spin disorder, Phys. Rev. B 99, 094304 (2019).

- [87] A. von Reppert, M. Mattern, J.-E. Pudell, S. P. Zeuschner, K. Dumesnil, and M. Bargheer, Unconventional picosecond strain pulses resulting from the saturation of magnetic stress within a photoexcited rare earth layer, Structural Dynamics 7, 024303 (2020).
- [88] M. Mattern, J.-E. Pudell, K. Dumesnil, A. von Reppert, and M. Bargheer, Towards shaping picosecond strain pulses via magnetostrictive transducers, Photoacoustics 30, 100463 (2023).
- [89] S. Günther, C. Spezzani, R. Ciprian, C. Grazioli, B. Ressel, M. Coreno, L. Poletto, P. Miotti, M. Sacchi, G. Panaccione, V. c. v. Uhlíř, E. E. Fullerton, G. De Ninno, and C. H. Back, Testing spin-flip scattering as a possible mechanism of ultrafast demagnetization in ordered magnetic alloys, Phys. Rev. B 90, 180407 (2014).
- [90] M. Richardson, D. Melville, and J. Ricodeau, Specific heat measurements on an Fe Rh alloy, Physics Letters A 46, 153 (1973).
- [91] I. A. Mogunov, S. Lysenko, F. Fernández, A. Rúa, A. V.

- Muratov, A. J. Kent, A. M. Kalashnikova, and A. V. Akimov, Photoelasticity of VO<sub>2</sub> nanolayers in insulating and metallic phases studied by picosecond ultrasonics, Phys. Rev. Mater. 4, 125201 (2020).
- [92] W. Singhsomroje and H. J. Maris, Generating and detecting phonon solitons in MgO using picosecond ultrasonics, Phys. Rev. B 69, 174303 (2004).
- [93] A. K. Vythelingum, T. Tremblais, D. B. Nguyen, D. Ourdani, E. Dandeu, V. Laude, C. Gourdon, and L. Thevenard, Role of coercivity in surface acoustic wave driven ferromagnetic resonance, ACS Applied Electronic Materials 7, 4055 (2025).
- [94] H. Wu, Q. Liu, R. Gao, S. Mi, L. Jia, J. Wang, H. Liu, S. Zhang, J. Wei, X. Wang, G. Han, and J. Wang, Acoustic wave-induced FeRh magnetic phase transition and its application in antiferromagnetic pattern writing and erasing, ACS Nano 18, 12134 (2024).